IOP Publishing Journal of Physics: Condensed Matter
J. Phys.: Condens. Matter **32** (2020) 205502 (13pp) https://doi.org/10.1088/1361-648X/ab680a

Magneto-conductivity of Weyl semimetals: the roles of inter-valley scattering and high-order Feynman diagrams

Lanting Feng, Tiancheng Ma and Yisong Zheng

Key Laboratory of Physics and Technology for Advanced Batteries (Ministry of Education), Department of Physics, Jilin University, Changchun 130012, People's Republic of China

E-mail: zys@jlu.edu.cn

Received 28 September 2019, revised 2 December 2019
Accepted for publication 6 January 2020
Published 18 February 2020

Abstract

Within the theoretical framework of Kubo formula and self-consistent Born approximation, we theoretically study the transversal and longitudinal magneto-conductivity of a type-I Weyl semimetal. We focus mainly on the peculiar role of inter-valley scattering on linear transversal magnetoresistance (LTMR) and negative longitudinal magnetoresistance (NLMR). At first, we find that the contributions of high-order Feynman diagrams to the transversal magneto-conductivity play the distinct roles between the cases of intra- and inter-valley scatterings. The former suppresses the transversal conductivity whereas the latter enhances it. Then, with the increase of scattering strength, the LTMR is destroyed, accompanying a sizable increase of transversal conductivity, in particular, in the case of the tilted cone. For longitudinal magneto-transport, inter-valley scattering contributes only trivial magnetoresistance. In contrast, intra-valley scattering is invalid for longitudinal magneto-transport which means a very large NLMR. In addition, the high-order Feynman diagrams always play the nontrivial role on the longitudinal conductivity even in the weak scattering limit. Finally, when altering the Fermi energy among low-lying Landau level, the peaks of transversal conductivity just correspond to the valleys of the longitudinal conductivity.

Keywords: Weyl semimetal, magnetoresistance, self-consistent Born approximation

(Some figures may appear in colour only in the online journal)

1. Introduction

Weyl semimetals represent an emerging class of topological materials which have drawn much attention in condensed matter physics and related fields. In a Weyl semimetal (WSM) the conduction and valence bands cross at discrete points within the Brillouin zone (BZ) [1]. And around each band-crossing point there appears Weyl-cone-like band structure, hence these points are called Weyl nodes. These Weyl nodes always appear in pairs of opposite chirality, which can be understood as monopoles and antimonopoles of Berry flux in momentum space. Weyl semimetals are uaually further classified into either time-reversal symmetry-breaking WSMs or inversion symmetry-breaking WSMs. In addition, WSMs can also be classified in terms of the degree of Weyl cone tilt which is allowed in realistic materials. Type-I WSMs have untilted or weakly tilted Weyl cone [2–4] with a point-like Fermi surface when it crosses the Weyl node. By contrast, type-II WSMs have over tilted and the Fermi surface appears as electron and hole pockets [5]. So far, experimentally verified WSM materials are exemplified by TaAs [6, 7], NbAs [8], TaP [9], and NbP [10]. Further promising candidates for WSMs include pyrochlore iridate [11], Heuslers [12–14], Mn_3Sn [15–17], Cd_3As_2 [18, 19], and so on.

Electronic transport properties in a WSM in the presence of a magnetic field are highly peculiar, owing to its topological nature of band structure. For recent theoretical studies, see, e.g. [11, 20–26] and references therein. The relevant theoretical anticipations include linear transversal magnetoresistance (LTMR) and negative longitudinal magnetoresistance

(NLMR) [27]. And the later is tightly associated with the chiral anomaly [22] of Weyl Fermions (Herein the terms 'transversal' and 'longitudinal' means that the electronic transport directions are perpendicular and parallel to the exerted magnetic field respectively). Both of LTMR and NLMR have thus far experimentally observed in realistic WSM materials [28–31]. In particular, some recent experimental articles have demonstrated them in the same materials [10, 18, 19, 29, 32–34]. Although electronic magneto-transport in WSMs has currently been a widely studied topic, to our knowledge, a comprehensive understanding on some key issues is still lacking, for example, the roles of inter-valley scattering and Weyl cone tilt. Some previous theoretical work employed a single-valley (one Weyl cone) model for simplicity. Inter-valley scattering is natively excluded in such a toy model, though, it captures the main characteristic of a Weyl Fermion. In realistic materials, inter-valley scattering (between Weyl cones) is inevitable. Thus, it is necessary to study the scattering between two different valleys. In addition, although Kubo formula provides an appropriate theoretical framework, and has thus far frequently employed to study the magneto-transport of WSM, the approximation is often restricted to lowest-order Feynman diagram which seems reasonable only in the weak scattering limit [35–37]. The higher-order-diagram contributions are thus ignored.

In the present work, we systematically study the transversal and longitudinal conductivities of WSM subject to a magnetic field, by using the Kubo formula within self-consistent Born approximation (SCBA) [21, 38, 39]. We find that the contributions of high-order Feynman diagrams to the transversal magneto-conductivity play the distinct roles between the cases of intra- and inter-valley scatterings. The former suppresses the transversal conductivity whereas the latter enhances it. For the longitudinal transport, the high-order Feynman diagrams play the nontrivial role on the longitudinal conductivity even in the weak scattering limit where the self-energy correction to the eigen-energy spectrum due to impurity scattering is far smaller than the Landau level spacing. In addition, inter-valley scattering contributes only trivial magnetoresistance. In contrast, intra-valley scattering is invalid for longitudinal magneto-transport which indicates a very large NLMR.

The paper is organized as follows. Section 2 is firstly devoted to an introduction to the Hamiltonian model of a type-I WSM. Then, starting from the theoretical framework of Kubo formula with SCBA, we derive the expressions of density of states (DOS) and conductivity of a WSM subject to intra- and inter-valley scattering respectively. In section 3, numerical results about the electronic magneto-transport are presented and discussed. Finally, we summarize our main findings in section 4.

2. Theory

We begin with a minimal Hamiltonian model which describes the low-energy electronic state in a WSM composed of a pair of Weyl node of opposite chirality. It is written as

$$\hat{H} = v_{\mathrm{f}}\hat{\boldsymbol{p}}\cdot\hat{\boldsymbol{\sigma}}\otimes\hat{\tau}_z + tv_{\mathrm{f}}\hat{p}_z\sigma_0\otimes\hat{\tau}_z + U(\boldsymbol{r})\sigma_0\otimes\hat{\tau}_0 + W(\boldsymbol{r})\sigma_0\otimes\hat{\tau}_x \tag{1}$$

where v_{f} is the fermi velocity of the Weyl-fermion-like conduction electron in the WSM; The parameter t denotes the degree of Weyl cone tilt in z direction. σ_i and τ_i with $i = x, y$, and z are pauli matrixes in spin and valley (two Weyl cones) spaces respectively; and $\sigma_0 = \tau_0$ is 2×2 identity matrix. In this Hamiltonian, we consider two opposite-tilted Weyl cones with the Weyl nodes located at $(0, 0, \pm Q)$ respectively; they are hence called the $\pm Q$ valleys hereafter. Obviously, in the right hand side of the above Hamiltonian, the first term describes two Weyl valleys without tilt, and the second is the tilt term. The third and last terms stand for, respectively, the intra-valley and inter-valley scattering potential. For convenience of theoretical treatment we assume the spatial parts of both the intra- and inter-valley scattering equally in a form of Dirac δ-function [38, 39], namely

$$U(\boldsymbol{r}) = W(\boldsymbol{r}) = \sum_{\lambda} u_{\lambda}^{i}\delta(\boldsymbol{r} - \boldsymbol{r}_{\lambda}^{i}) \tag{2}$$

where u_{λ}^{i} is the amplitude of the scattering potential created by an impurity at $\boldsymbol{r}_{\lambda}^{i}$. Such a simple scattering potential model captures most physical properties of quantum transport, though it looks unrealistic. And it has been extensively employed for theoretical studies of electronic transport property in solids with various typical band structures. To explore the magneto-transport property of a WSM, we introduce a magnetic field with strength B in z direction, i.e. parallel to the connecting line between the two nodes, which enters the above Hamiltonian simply via the peierls substitution: $\hat{\boldsymbol{p}} \Rightarrow \hat{\boldsymbol{p}} + e\boldsymbol{A}/c$, with the vector potential $\boldsymbol{A}(\boldsymbol{r}) = (-By, 0, 0)$.

For a perfect WSM, i.e. in the absence of any impurity scattering, the two Weyl valleys are decoupled. Then, the above Hamiltonian in the presence of the magnetic field have analytical eigensolutions. The eigen-energy exhibits the one-dimensional subbands and the Landau level (LL) spectrum, respectively, in the directions parallel and perpendicular to the magnetic field. It has an analytical expression as [27]

$$E(\alpha, n, p_z) = \begin{cases} \alpha v_{\mathrm{f}}\big(tp_z + \frac{n}{|n|}\frac{1}{l_B}\sqrt{2|n| + l_B^2 p_z^2}\,\big) & |n| > 0 \\ \alpha v_{\mathrm{f}} p_z(t-1) & n = 0 \end{cases} \tag{3}$$

with $l_B = (eB/c\hbar)^{-\frac{1}{2}}$ is the magnetic length. Here α and n are the indexes of the valley parity and Landau level respectively, $\alpha = \pm$ for $\pm Q$ valleys. What is special is that the $n = 0$ LL has a unidirectional and constant band velocity in either valley which reflects the chiral anomaly. Corresponding to the above eigen-energy, the eigenstate takes a form of four-component spinor which can be written in a compact form as

$$|\alpha, n, p_x, p_z\rangle = \begin{pmatrix} \theta(\alpha Q)u_n(\zeta)\phi_{|n|-1}(\xi) \\ \theta(\alpha Q)d_n(\zeta)\phi_{|n|}(\xi) \\ \theta(-\alpha Q)u_n(\zeta)\phi_{|n|-1}(\xi) \\ \theta(-\alpha Q)d_n(\zeta)\phi_{|n|}(\xi) \end{pmatrix} |p_x\rangle|p_z\rangle. \tag{4}$$

In the above expression the function $\theta(x) = 1$ for $x > 0$ and $\theta(x) = 0$ otherwise. $\phi_{|n|}(\xi)$ with $\xi = l_B^{-1}y - l_B p_x/\hbar$ is

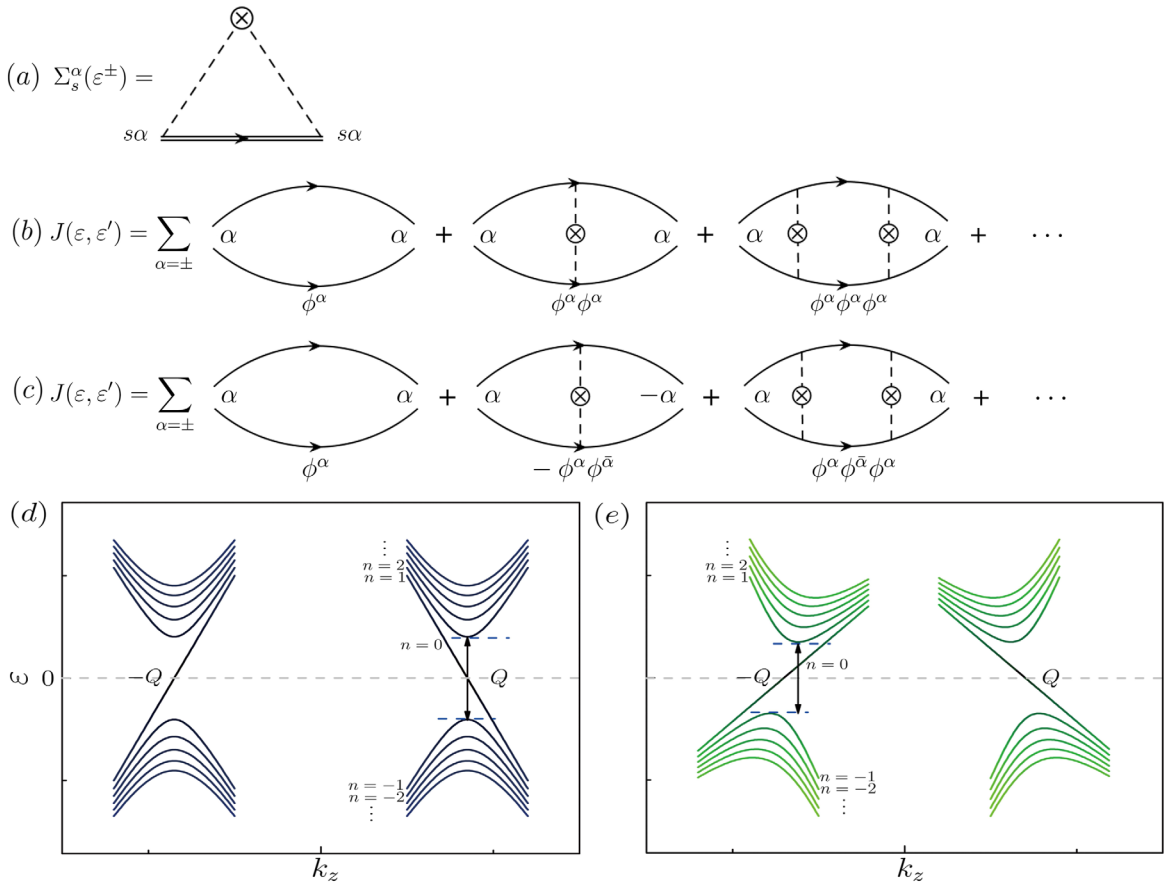

Figure 1. (a) Feynman diagram of electronic self-energy in SCBA. The double lines with arrow denotes the dressed Green function, and the dashed lines denote the impurity potential. The notation $\otimes$ means the procedure of impurity configuration average. (b) Feynman diagram of the quantity $J(\varepsilon,\varepsilon')$ in the presence of intra-valley scattering. Except the first one, the remaining bubble diagrams are called the vertex corrections. (c) Feynman diagram of the quantity $J(\varepsilon,\varepsilon')$ in the presence of inter-valley scattering. Noting the even-numbered bubble diagrams have the opposite sign to the odd-numbered ones. (d) and (e) Dispersions of low energy Landau subbands for (d) untilted ($t = 0.0$) and (e) tilted WSMs ($t = 0.5$) which consists of a pair of Weyl nodes with opposite chirality and tilt vector located at (0, 0, $\pm$ Q) respectively.

the normalized eigenfunctions of 1D harmonic oscillator. Besides, $u_n(\zeta) = \theta(npz)\cos(\frac{\zeta}{2}) + \theta(-npz)\sin(\frac{\zeta}{2})$ and $d_n(\zeta) = \theta(-npz)\cos(\frac{\zeta}{2}) - \theta(npz)\sin(\frac{\zeta}{2}) + (1-\theta(|n|))$ with $\zeta = \arctan[\sqrt{2|n|}/(l_B p_z/\hbar)]$.

To study the magneto-transport of electrons in a WSM within the theoretical framework of quantum transport, we employ the Kubo-Bastin formula [40, 41] which expresses the diagonal conductivity in terms of Green functions. At zero temperature it is given by

$$\sigma_{xx(zz)}(\varepsilon) = \frac{e^2\hbar}{\pi V}\left\langle \mathrm{Tr}[\hat{v}_{x(z)}\mathrm{Im}\hat{G}(\varepsilon^+)\hat{v}_{x(z)}\mathrm{Im}\hat{G}(\varepsilon^+)]\right\rangle \quad (5)$$

where V denotes the volume of the system and $\hat{v}_{x(z)}$ is the component of velocity operator. For the WSM described by the above Hamiltonian, we have $\hat{v}_{x(z)} = v\sigma_{x(z)} \otimes \tau_z$. The operators of retarded and advanced Green functions are defined as $\hat{G}(\varepsilon^{\pm}) = [\varepsilon - \hat{H} \pm \mathrm{i}\eta]^{-1}$ with ε and η being the Fermi energy and a positive infinitesimal respectively. And finally $\langle\cdots\rangle$ in equation (5) stands for an averaging over impurity configurations. For the theoretical model of WSM under our consideration, σ_{xx} and σ_{zz} are called the transversal and longitudinal conductivity, since they are perpendicular and parallel to the magnetic field direction respectively.

Prior to explore the effect of impurity scattering, we would like to work out the transversal and longitudinal conductivities of the perfect WSM (in the absence of any scattering potential) in terms of the eigensolution given above. Considering that the Green functions are diagonal in the eigen representation of a perfect WSM, after a straightforward derivation we have

$$\sigma_{xx} = \frac{e^2\hbar}{4\pi^3 l_B^2} v_{\mathrm{f}}{}^2 \sum_{\alpha,n,n'} \int \mathrm{d}p_z [u_{n'}{}^2(\zeta) d_n{}^2(\zeta)\delta_{|n|,|n'|-1} + u_n{}^2(\zeta) d_{n'}{}^2(\zeta)\delta_{|n|,|n'|+1}] \times \frac{\eta}{[\varepsilon - E(\alpha,n,p_z)]^2 + \eta^2}\frac{\eta}{[\varepsilon - E(\alpha,n',p_z)]^2 + \eta^2} \quad (6)$$

and

$$\sigma_{zz} = \frac{e^2\hbar}{4\pi^3 l_B^2} v_{\mathrm{f}}{}^2 \sum_{\alpha,n} \int \{[u_n^2(1+t) + d_n^2(-1+t)] \frac{\eta}{[\varepsilon - E(\alpha,n,p_z)]^2 + \eta^2}\}^2 \mathrm{d}p_z. \quad (7)$$

In addition, the corresponding DOS of the perfect WSM can be expressed as

$$\rho(\varepsilon) = -\frac{1}{\pi V}\mathrm{Tr}\mathrm{Im}G(\varepsilon + \mathrm{i}\eta) = \frac{1}{4\pi^3 l_B^2}\sum_{\alpha,n}\int \frac{\eta}{[\varepsilon - E(\alpha,n,p_z)]^2 + \eta^2}\mathrm{d}p_z. \quad (8)$$

It will be seen below that these expressions are helpful for us to understand the numerical result of the conductivity spectrum in the presence of impurity scattering, in particular, in the case of relatively weak scattering.

Now let us deal with impurity scattering. The presence of impurity scattering complicates the theoretical treatment of the magneto-conductivity since it brings about the nontrivial self-energy to Green function and the vertex correction to the conductivity. We adopt the SCBA to incorporate the impurity scattering into the formula of the diagonal conductivity of a WSM which can provide us with a reasonable result in the case of weak scattering. Within the SCBA the self-energy operator satisfies

$$\hat{\Sigma}(\varepsilon \pm \mathrm{i}\eta) = \langle \hat{U}\hat{G}(\varepsilon \pm \mathrm{i}\eta)\hat{U}\rangle \quad (9)$$

and the Green function operator can be expressed in a form as

$$\hat{G}(\varepsilon \pm \mathrm{i}\eta) = [\varepsilon \pm \mathrm{i}\eta - \hat{H}_0 - \hat{\Sigma}(\varepsilon \pm \mathrm{i}\eta)]^{-1} \quad (10)$$

where $\hat{H}_0$ is the Hamiltonian of the perfect WSM, i.e. the Hamiltonian given by equation (1) with the impurity scattering part excluded. Equations (9) and (10) form a closed relationship between the Green function and self-energy. However, they should be recasted into matrix forms in a given representation in order to perform numerical calculations. Instead of the aforementioned eigen representation, it proves to be convenient to use the LL representation [38, 39] for relevant formulations. The LL basis is denoted as $|\alpha\, s, m\, p_x\, p_z\rangle$ with m bing the index of conventional LL state and $s = \uparrow$ or $\downarrow$ the index of pseudospin. For example, in Q-valley there are two such basis states: $|+\uparrow, m\, p_x\, p_z\rangle = (\phi_m(\xi), 0, 0, 0)^T|p_x\rangle|p_z\rangle$ and $|+\downarrow, m\, p_x\, p_z\rangle = (0, \phi_m(\xi), 0, 0)^T|p_x\rangle|p_z\rangle$. The averaging over impurity configuration restores the translational symmetry. Accordingly, the Green function and self-energy become diagonal with respect to momentum eigenvalues p_x and p_z. Moreover, it is not difficult to find that within the SCBA the Green function and self-energy are both α-diagonal. In particular, in LL representation the matrix element of self-energy is independent of m, p_x and p_z. And the matrix element of Green function is independent of p_x. In such a context, we introduce the shorthands $\Sigma_s^\alpha(\varepsilon^\pm) = \langle\alpha, s, m, p_x, p_z|\hat{\Sigma}(\varepsilon \pm \mathrm{i}\eta)|\alpha, s, m, p_x, p_z\rangle$ and $G^\alpha_{ms,m's'}(\varepsilon^\pm, p_z) = \langle\alpha, s, m, p_x, p_z|\hat{G}(\varepsilon \pm \mathrm{i}\eta)|\alpha, s', m', p_x, p_z\rangle$. As a result, the self-energy equation given by equation (9) is recasted into a form as

$$\Sigma_s^\alpha(\varepsilon^\pm) = \frac{A_i\hbar^2 v_\mathrm{f}^2}{16\pi^3 l_B^2 q_0}\sum_m \int G^{\alpha'}_{ms,ms}(\varepsilon^\pm, p_z)\mathrm{d}p_z. \quad (11)$$

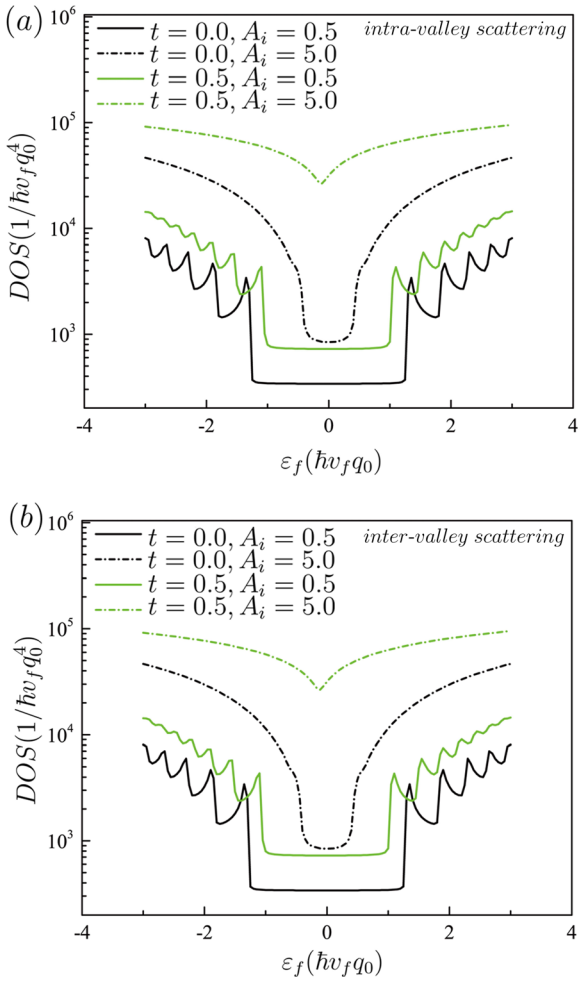

Figure 2. DOS of WSM for the cases with different cone tilts and scattering strengths. (a) and (b) Show the cases of intra- and inter-valley scattering respectively.

Such an expression is also illustrated by the Fenyman diagram given by figure 1(a). Note that in equation (11) the valley index of Green function $\alpha' = \alpha$ for intra-valley scattering but $\alpha' = -\alpha$ for inter-valley scattering. To measure the scattering strength, we have introduced a dimensionless parameter $A_i = 4\pi n_i \bar{u}_i^2 q_0/(\hbar^2 v_\mathrm{f}^2)$ with n_i the impurity concentration and $\bar{u}_i^2$ the squared average of impurity potential strength. Note that here we introduce the reference electronic wavevector q_0 for convenience. Furthermore, we find that the Green function matrix in LL representation is block-diagonal which takes a form as

$$\begin{bmatrix} G^\alpha_{m-1\uparrow,m-1\uparrow}(\varepsilon^\pm, p_z) & G^\alpha_{m-1\uparrow,m\downarrow}(\varepsilon^\pm, p_z) \\ G^\alpha_{m\downarrow,m-1\uparrow}(\varepsilon^\pm, p_z) & G^\alpha_{m\downarrow,m\downarrow}(\varepsilon^\pm, p_z) \end{bmatrix} = \begin{bmatrix} \varepsilon^\pm - \alpha(1+t)v_\mathrm{f}p_z - \Sigma^\alpha_\uparrow(\varepsilon^\pm) & \frac{\alpha v_\mathrm{f}}{l_B}\sqrt{2m} \\ \frac{\alpha v_\mathrm{f}}{l_B}\sqrt{2m} & \varepsilon^\pm - \alpha(-1+t)v_\mathrm{f}p_z - \Sigma^\alpha_\downarrow(\varepsilon^\pm) \end{bmatrix}^{-1}. \quad (12)$$

We have thus established the iterative equations, i.e. equations (11) and (12), for solving self-consistently the Green function and self-energy.

Within the SCBA, the DOS of the WSM in the presence of impurity scattering can be written as

$$\rho(\varepsilon) = -\frac{1}{\pi V}\mathrm{Tr}\mathrm{Im}G(\varepsilon + \mathrm{i}\eta) = -\frac{1}{\pi n_i \bar{u}_i^2}\sum_{\alpha s}\mathrm{Im}\Sigma_s^{\alpha}(\varepsilon). \quad (13)$$

We now turn to treat magneto-conductivity of a WSM within SCBA. Firstly, starting form equation (5), we derive out an expression about the transversal conductivity subject to intra- or inter-valley scattering which is given by

$$\sigma_{xx} = \frac{e^2\hbar}{4\pi V}[J(\varepsilon^+,\varepsilon^-) + J(\varepsilon^-,\varepsilon^+) - J(\varepsilon^+,\varepsilon^+) - J(\varepsilon^-,\varepsilon^-)]. \quad (14)$$

In the above expression the quantity $J(\varepsilon,\varepsilon')$ represents a summation over a series of bubble diagrams, as shown in figures 1(b) and (c) for the cases of intra-valley and inter-valley scattering respectively. For the case of intra-valley scattering we have

$$J(\varepsilon,\varepsilon') = \frac{4\pi q_0 V}{A_i\hbar^2}\sum_{\alpha}[\frac{\phi^{\alpha}(\varepsilon,\varepsilon')}{1-\phi^{\alpha}(\varepsilon,\varepsilon')} + \frac{\phi^{\alpha}(\varepsilon',\varepsilon)}{1-\phi^{\alpha}(\varepsilon',\varepsilon)}] \quad (15)$$

with

$$\phi^{\alpha}(\varepsilon,\varepsilon') = \frac{A_i\hbar^2 v_{\mathrm{f}}^2}{16\pi^3 l_B^2 q_0}\sum_{n}\int G^{\alpha}_{n+,n+}(\varepsilon,p_z)G^{\alpha}_{n-,n-}(\varepsilon',p_z)\mathrm{d}p_z. \quad (16)$$

For the case of inter-valley scattering we have

$$J(\varepsilon,\varepsilon') = \frac{4\pi q_0 V}{A_i\hbar^2}\sum_{\alpha}\left\{\frac{\phi^{\alpha}(\varepsilon,\varepsilon')[1-\phi^{\bar{\alpha}}(\varepsilon,\varepsilon')]}{1-\phi^{\alpha}(\varepsilon,\varepsilon')\phi^{\bar{\alpha}}(\varepsilon,\varepsilon')} + \frac{\phi^{\alpha}(\varepsilon',\varepsilon)[1-\phi^{\bar{\alpha}}(\varepsilon',\varepsilon)]}{1-\phi^{\alpha}(\varepsilon',\varepsilon)\phi^{\bar{\alpha}}(\varepsilon',\varepsilon)}\right\} \quad (17)$$

where $\phi^{\alpha(\bar{\alpha})}(\varepsilon,\varepsilon')$ obeys formally the same definition as the case of intra-valley scattering, but the Green functions therein must be replaced with the ones corresponding to inter-valley scattering. In equation (17) the shorthand $\bar{\alpha} = -\alpha$ has been used for compactness. In comparison with the case of intra-valley scattering we find that the bubble diagrams corresponding to the inter-valley scattering consist of two kinds, as shown in figure 1(c). The diagrams of the first kind describe the scattering processes with the initial and final states belonging to the same valley, though another valley takes part into the scattering as intermediate states. In contrast, the diagrams of second kind refer to the scattering processes between the opposite valleys.

The formulas of the longitudinal conductivity follow the analogous form as the transversal conductivity. But the quantity $J(\varepsilon,\varepsilon')$ should be redefined. For intra-valley scattering, $J(\varepsilon,\varepsilon')$ occurring in σ_{zz} is given by

$$J(\varepsilon,\varepsilon') = \frac{4\pi q_0 V}{A_i\hbar^2}\sum_{\alpha}(v_z^{\alpha})\{[M^{\alpha}]^{-1} - [\boldsymbol{I}]\}^{-1}(v_z^{\alpha})^T \quad (18)$$

with $\boldsymbol{I}$ is the 2×2 identity matrix, and velocity vector is defined as

$$(v_z^{\alpha}) = (\alpha(1+t)v_{\mathrm{f}}, \quad \alpha(-1+t)v_{\mathrm{f}}) \quad (19)$$

and

$$[M^{\alpha}] = \begin{bmatrix}\phi_{11}^{\alpha}(\varepsilon,\varepsilon') & \phi_{12}^{\alpha}(\varepsilon,\varepsilon')\\ \phi_{21}^{\alpha}(\varepsilon,\varepsilon') & \phi_{22}^{\alpha}(\varepsilon,\varepsilon')\end{bmatrix} \quad (20)$$

with

$$\phi_{11}^{\alpha}(\varepsilon,\varepsilon') = \frac{A_i\hbar^2 v_{\mathrm{f}}^2}{16\pi^3 l_B^2 q_0}\sum_{m}\int G^{\alpha}_{m\uparrow,m\uparrow}(\varepsilon,p_z)G^{\alpha}_{m\uparrow,m\uparrow}(\varepsilon',p_z)\mathrm{d}p_z \quad (21)$$

$$\phi_{12}^{\alpha}(\varepsilon,\varepsilon') = \phi_{21}^{\alpha}(\varepsilon',\varepsilon) = \frac{A_i\hbar^2 v_{\mathrm{f}}^2}{16\pi^3 l_B^2 q_0}\sum_{m}\int G^{\alpha}_{m+1\downarrow,m\uparrow}(\varepsilon,p_z)G^{\alpha}_{m\uparrow,m+1\downarrow}(\varepsilon',p_z)\mathrm{d}p_z \quad (22)$$

$$\phi_{22}^{\alpha}(\varepsilon,\varepsilon') = \frac{A_i\hbar^2 v_{\mathrm{f}}^2}{16\pi^3 l_B^2 q_0}\sum_{m}\int G^{\alpha}_{m\downarrow,m\downarrow}(\varepsilon,p_z)G^{\alpha}_{m\downarrow,m\downarrow}(\varepsilon',p_z)\mathrm{d}p_z. \quad (23)$$

For inter-valley scattering, $J(\varepsilon,\varepsilon')$ is redefined as

$$J(\varepsilon,\varepsilon') = \frac{4\pi q_0 V}{A_i\hbar^2 v_{\mathrm{f}}^2}\left[\begin{pmatrix}v_z^+ & v_z^-\end{pmatrix}\left\{\begin{bmatrix}M^+ & \\ & M^-\end{bmatrix}^{-1} - \begin{bmatrix}M^- & \\ & M^+\end{bmatrix}\right\}^{-1}\begin{pmatrix}v_z^+\\ v_z^-\end{pmatrix} + \begin{pmatrix}v_z^+ & v_z^-\end{pmatrix}\left\{\begin{bmatrix}M^+ & \\ & M^-\end{bmatrix}^{-1} - \begin{bmatrix}M^- & \\ & M^+\end{bmatrix}\right\}^{-1}\begin{bmatrix}M^- & \\ & M^+\end{bmatrix}^{-1}\begin{pmatrix}v_z^-\\ v_z^+\end{pmatrix}\right] \quad (24)$$

where $[v_z^{\alpha}]$ and $[M^{\alpha}]$ obey the same definition as given by equations (19) and (20)–(23).

3. Numerical results and discussions

With the above theoretical treatment of the conductivity within the SCBA, we are now ready to perform numerical calculations about the transversal and longitudinal conductivity, by which we can study the influence of intra- and inter-valley scattering

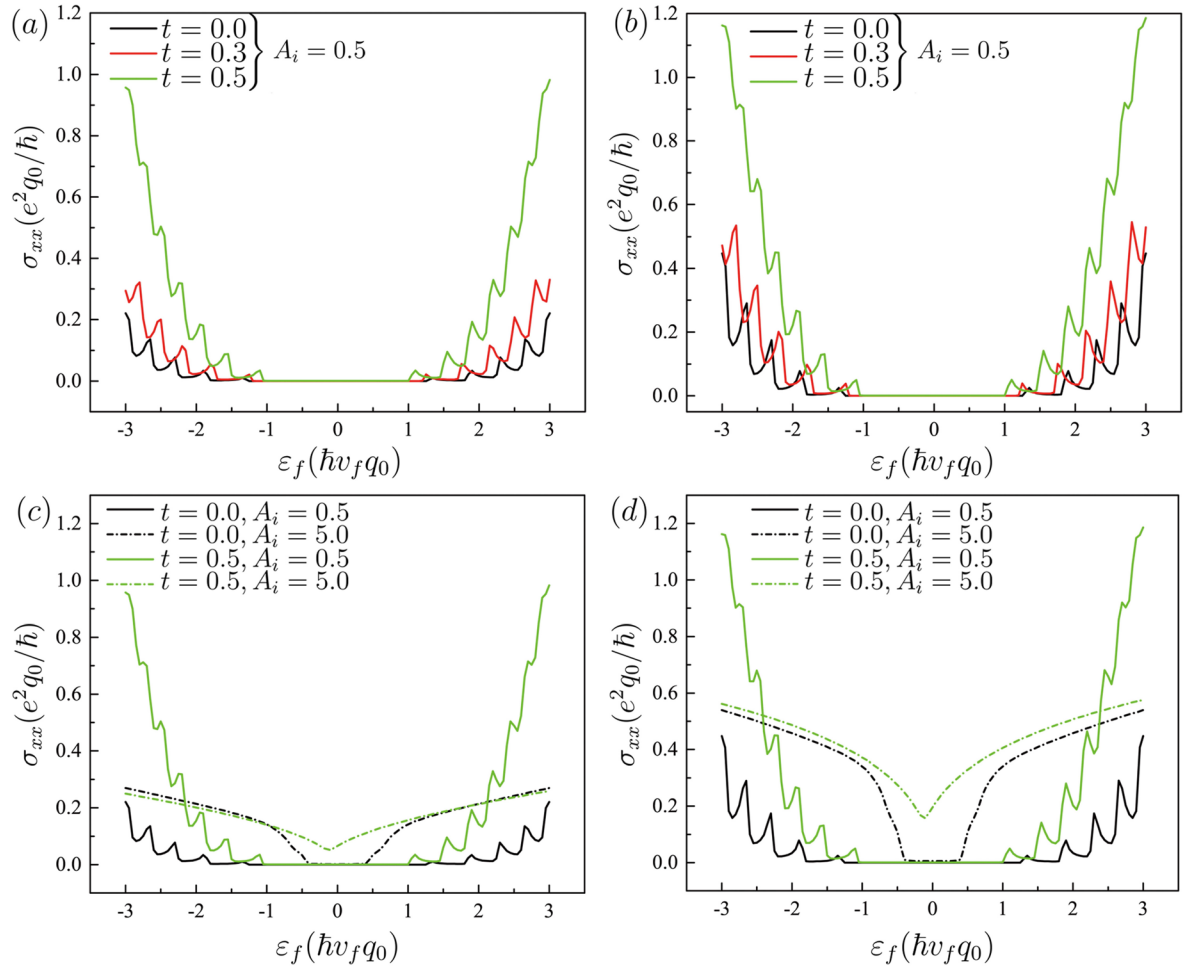

Figure 3. Transversal conductivity of a WSM for typical cases. (a) Weak intra-valley scattering ($A_i = 0.5$) with different cone tilts of $t = 0.0$, 0.3 and 0.5. (b) Same as (a) but for the case of inter-valley scattering. (c) A comparison of σ_{xx} spectra between strong and weak intra-valley scattering ($A_i = 0.5$ and 5.0), without and with cone tilt ($t = 0$ and 0.5). (d) Same as (c) but for the case of inter-valley scattering.

on the quantum magneto-transport of electrons in WSM. Before to proceed, we set the units $\hbar = e = v_f = q_0 = 1$ for convenience of numerical calculations. Note that we have introduced the reference electronic wavevector q_0. And $|Q| = q_0 = 1$ is implied unless declared otherwise. In addition, we specify the size of the BZ as $-50q_0 < p_{x(z)} < 50q_0$ which is used when calculating the integration over the electronic momentum p_x and p_z. We also need to truncate the summation over the LL index within a maximal but finite cutoff value N_m. We find that a cutoff $N_m = 300$ is enough to guarantee the convergence of the calculated spectrum of conductivity in the low energy region around the nodal energy of WSM. Last but not least, we have to emphasize that in this work we only consider the magneto-transport of type-I WSM. This is because that the type-II WSM, i.e. the case of $|t| > 1$ in our Hamiltonian, has unclosed fermi surface. When neither the electronic or hole pocket meets the fictitious BZ boundary, the numerical result of the conductivity becomes unreliable.

First of all, the numerical results of the DOS spectrum are shown in figure 2 for typical cases with different Weyl cone tilts and impurity scattering strengths. We can see that as the impurity scattering is very weak, e.g. the cases of $A_i = 0.5$ in figures 2(a) and (b), the DOS spectra exhibit clearly a series of peaks, regardless of intra- or inter-valley scattering. And these peaks occur whenever the energy passes through the minima of $n \neq 0$ subbands. The central flat bottom but with a nonzero value is contributed by chiral $n = 0$ subbands. According to the eigen energy spectrum, the width of the flat bottom is proportional to the magnetic field strength. The multiple peak profile of these DOS spectra reflects the 1D subband structure of WSM induced by a magnetic field. However, these DOS peaks disappear in the case of strong impurity scattering, as shown in figure 2 for the case of $A_i = 5.0$. This is owing to the smearing effect caused by the imaginary part of the non-trivial self-energy of strong scattering. All these features of DOS spectrum of a WSM in the presence of a magnetic field is previously reported in some theoretical study [42, 43]. But the impurity scattering considered therein is restricted in the intra-valley scattering. And no cone tilt was involved. Therefore, our calculation indicates that the inter-valley scattering has a very similar effect as the intra-valley scattering on the DOS spectrum of WSM. In addition, as the Weyl cone gets tilted, the DOS spectrum has an appreciable rise, in comparison with the counterpart of untilted WSM. From figures 1(d) and (e)

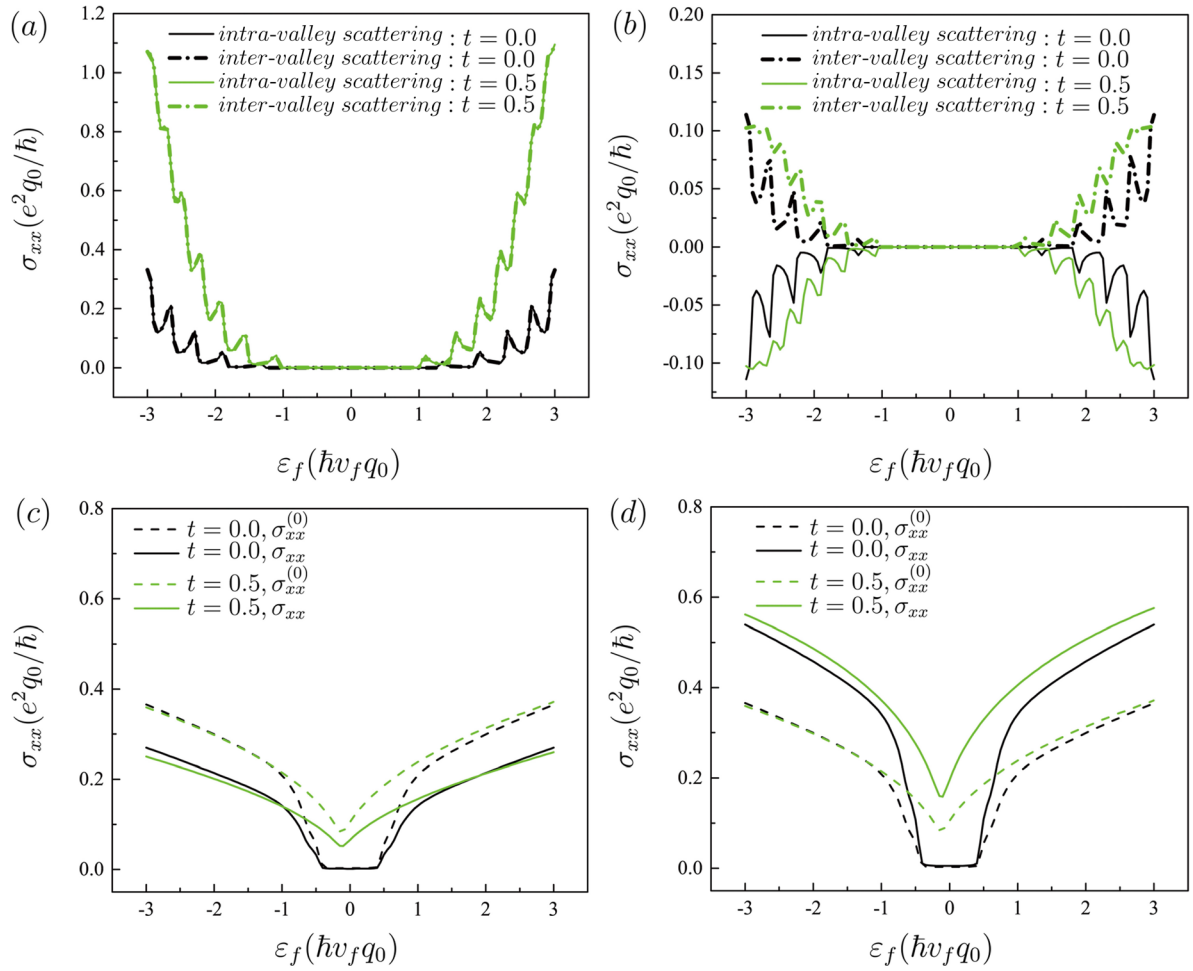

Figure 4. (a) A comparison of the contributions of the zero-order bubble diagrams to transverse conductivity spectra between the cases of intra- and inter-valley scattering. (b) Is similar to (a) but herein the contribution of the first-order bubble diagrams to transversal conductivity are compared. (c) σ_{xx} and the contribution of the zero-order bubble diagram to it (σ^0_{xx}) are compared for the cases with and without cone tilts, subject to strong intra-valley scattering. (d) Is similar to (c) but for the case of inter-valley scattering.

one can see that the low-lying subbands look also tilted for the tilted WSM. As a result, both of the electronic band velocity and the subband spacings diminish, which can well account for the enhancement of the DOS as the cone gets tilted.

The spectra of transversal conductivity, i.e. σ_{xx} versus ε_f, for different cases are shown in figure 3. In the case of weak impurity scattering, e.g. the case of $A_i = 0.5$ as shown in figures 3(a) and (b), the σ_{xx} spectra subject to intra- and inter-valley scattering have similar features. First, all these conductivity spectrum present a series of peaks which are aligned in energy with the peaks of corresponding DOS spectra shown in figure 2. Then, σ_{xx} increases with the Weyl cone tilt, bearing an analogy with the DOS spectra shown in figure 2. The expression of σ_{xx} for a clear WSM, i.e. equation (6) is instructive for us to understand these observed features of conductivity. In weak scattering limit, the impurity scattering self-energy is much smaller than the subband spacings. In this context, it is reasonable to consider equation (6) as an approximation of σ_{xx}. We can see that the imaginary part of Green function appears in equation (6), similar to the expression of DOS as given by equation (8). Therefore, it is not surprising that both of the spectra of DOS and σ_{xx} exhibits the same features as mentioned above. In figures 3(c) and (d) we compare σ_{xx} spectrum between the cases of weak and strong scattering. A general feature, regardless of neither the cone tilt or intra- and inter-valley scattering, is that σ_{xx} increases with the scattering strength in the low energy region. This is a reasonable result since the impurity scattering shifts the mobility edge, making the region of extended state around each LL broadening which brings about the increase of transversal conductivity.

By comparing the conductivity spectra as shown in figures 3(c) and (d), it can be seen that with the same scattering strength σ_{xx} in the case of inter-valley scattering is larger than that in the case of intra-valley scattering. By a detailed analyse, we find that this result arises from the distinct contributions of high-order bubble diagrams between the intra- and inter-valley scattering. If we take only account of the contribution of the zero-order bubble diagram to the transversal conductivity, as shown in figure 4(a), the conductivity does not show appreciable difference between the cases of intra- and inter-valley scattering. However, as shown in figure 4(b), the first-order diagram, namely, the bubble diagram with one impurity line as illustrated in figures 1(b) and (c), give a negative contribution

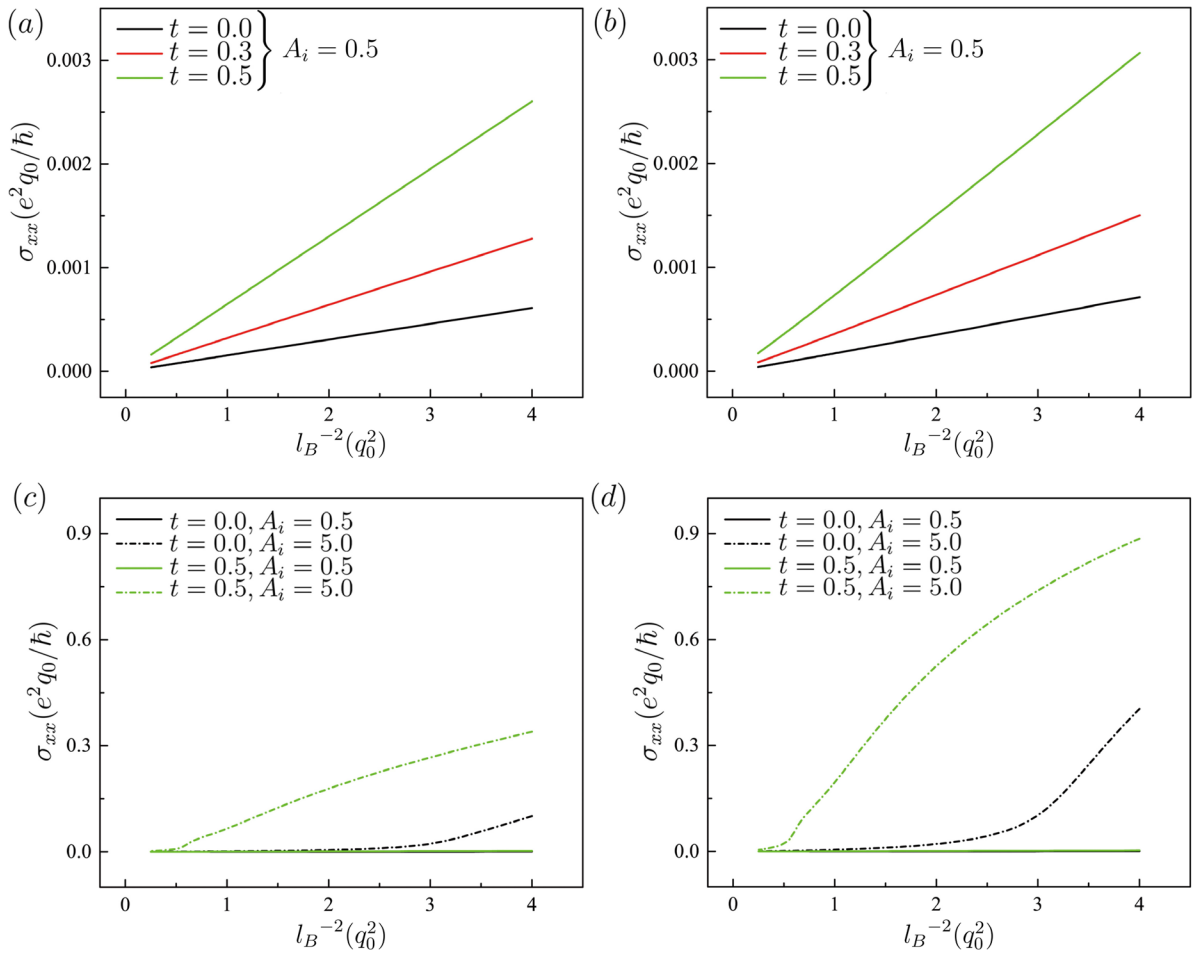

Figure 5. σ_{xx} versus l_B^{-2} (proportional to magnetic field strength) at zero energy ($\varepsilon_f = 0.0$). (a) Weak intra-valley scattering of $A_i = 0.5$ for the cases of cone tilt $t = 0.0$ and 0.3 and 0.5. (b) Same as (a) but for the cases of weak inter-valley scattering. (c) A comparison of σ_{xx} versus l_B^{-2} between the cases of weak and strong intra-valley scattering. (d) Same as (c) but for the cases of inter-valley scattering.

to σ_{xx} in the case of intra-valley scattering. On the contrary, the contribution of first-order bubble diagram of inter-valley scattering is positive. Hence it further enhances the value of σ_{xx} from the zero-order bubble diagram. In view of very weak scattering for the cases shown in figures 4(a) and (b), the contribution of the first-order bubble diagram to σ_{xx} is smaller than the contribution of zero-order bubble diagram by about one order of magnitude, though, they have opposite modifications to σ_{xx} for the intra- and inter-valley scattering. However, with the increase of scattering strength, the contributions beyond zero-order diagram is expected to become important. In figures 4(c) and (d), the whole σ_{xx} and the contribution to it of the zero-order bubble diagram are compared for the case of relatively strong scattering. We can see that the high-order bubble diagrams have nontrivial contributions indeed, no matter whether the cone tilts or not. And the high-order bubble diagrams have just the opposite contributions to σ_{xx} between the cases of intra- and inter-valley scattering. The former suppresses the transversal conductivity whereas the latter enhances it. Our results show that for transversal conductivity, the inter-valley scattering does not show distinct effect from intra-valley scattering, though the former results in a relative weak conductivity than the latter does if both have the same strength. This result agrees with the anticipation given in [42] where the inter-valley scattering was excluded. However, it will be seen below that the inter-valley scattering plays the distinct role on the longitudinal magnetotransport. It provides the system with finite resistivity while the intra-valley scattering become invalid to affect the electronic transport.

We now calculate the transversal conductivity as a function of magnetic field strength (proportional to l_B^{-2}) at zero energy($\varepsilon_f = 0$). The numerical results are shown in figure 5 for various cases. In the case of weak scattering, whether it is intra-valley or inter-valley scattering, as shown in figures 5(a) and (b) respectively, the conductivity depends linearly on magnetic field strength. This result can be understood from equation (6). At $\varepsilon_f = 0$, the $n = 0$ Landau level dominates the term after summation over n and n' which is thereby almost independent of magnetic field strength. Consequently, σ_{xx} has a linear dependence on l_B^{-2}. Moreover, as observed in figures 5(a) and (b), σ_{xx} tends to zero as the magnetic field gets weak. Such a feature was also pointed out in previous theoretical study [42]. However, the Hall conductivity takes a nonzero value even in the absence of a magnetic field because of the anomalous Hall effect in WSM. Therefore, when the magnetic field becomes weak enough, we have $\sigma_{xx} \ll \sigma_{xy}$,

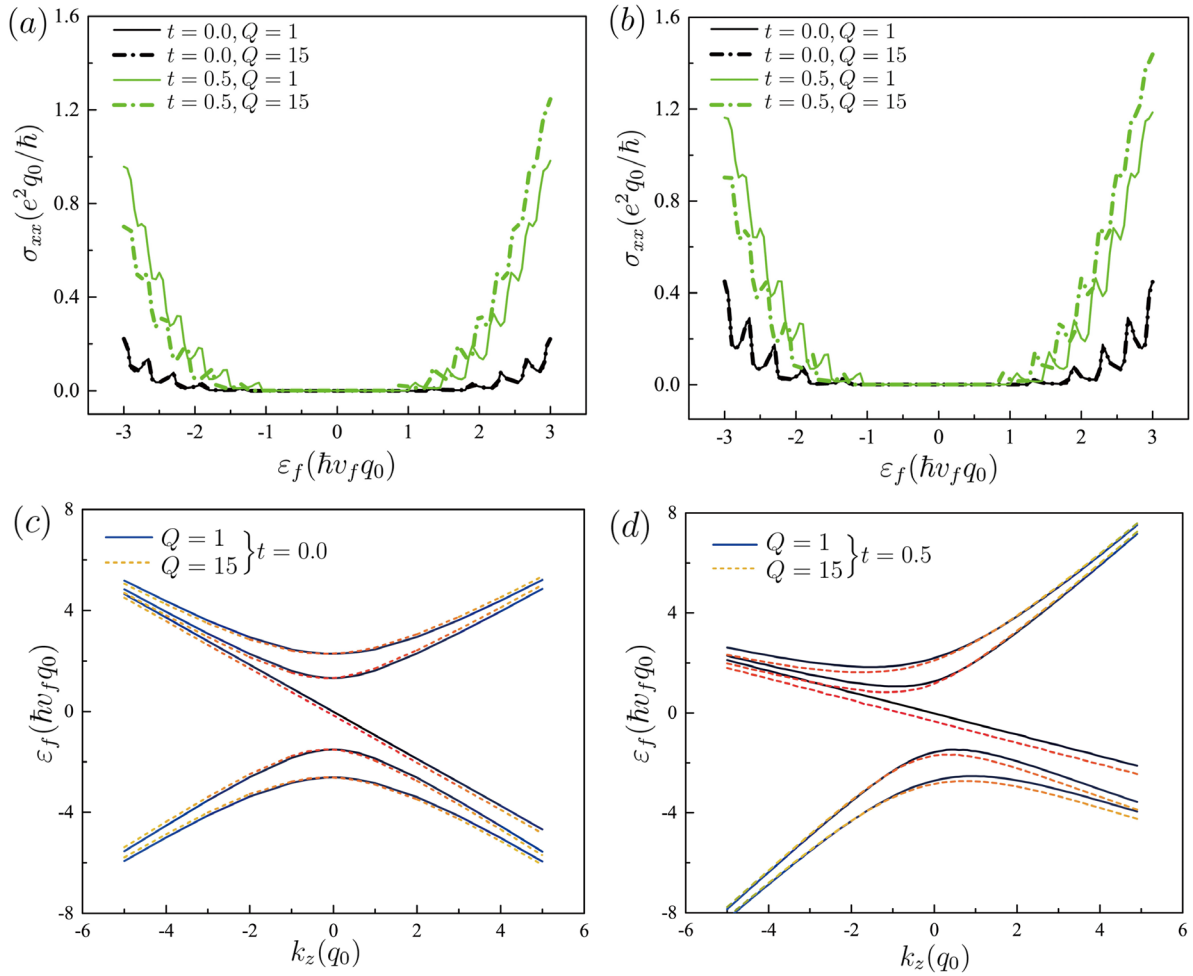

Figure 6. A comparison of σ_{xx} or energy spectrum between $Q = 1$ and $Q = 15$ ($2Q$ is the interval between two Weyl nodes in k_z direction of the BZ). (a) and (b) Shows σ_{xx} versus ε_f in the cases of intra- and inter-valley scattering respectively without and with cone tilt ($t = 0$ and 0.5). (c) and (d) Shows the modification to the eigen energy spectrum by the impurity scattering in the case of intra-valley scattering with $t = 0$ and 0.5 respectively.

which we refer to as the weak magnetic field limit. In such a situation, we have $\rho_{xx} = \frac{\sigma_{xx}}{\sigma_{xx}^2+\sigma_{xy}^2} \approx \frac{\sigma_{xx}}{\sigma_{xy}^2}$. Namely, the diagonal resistivity is proportional to the diagonal conductivity. As a result, the linear $\sigma_{xx} \sim l_B^{-2}$ relation shown in figures 5(a) and (b) implies the LTMR in the weak magnetic field limit. Besides, we can see that, with the increasing of the cone tilt, the conductivity increases rapidly. This indicates that the tilted WSM has larger LTMR. More importantly, we can see in figures 5(c) and (d) that the increase of scattering strength destroys the linear $\sigma_{xx} \sim l_B^{-2}$ relation notably, meanwhile, with a significant enhancement of σ_{xx}, regardless of intra- and inter-valley scattering. We notice that similar results were previously obtained, e.g. in [44] where the transversal conductivity calculated by scattering matrix approach decreases with the increase of magnetic field strength at the strong disorder limit.

In figure 6 we compare σ_{xx} spectra by altering the value of Q ($2Q$ is the interval between two Weyl nodes in k_z direction of the BZ). Comparing with figures 6(a) and (b), we can see that the variation of conductivity with Q is very similar in both intra-valley scattering and inter-valley scattering. When the Weyl cone is not tilted ($t = 0$), $Q = 1$ and $Q = 15$ of the conductivity curves are the same, however, when the tilt is not 0 ($t \neq 0$), they are obviously different. We can see that it is easy to distinguish the conductivity of large Q from that of small Q if the Weyl cone is tilted. By comparing the subband strutures as shown in figures 1(d) and (e), we can find that the cone tilt makes the Landau subbands of two valleys declined toward the BZ center. As a result, the eigen energies of the states near the BZ boundary move up. And these states are truncated at the BZ boundary center. Due to impurity scattering, these states play an important role to modify the eigen energy near the Fermi level. In particular, for the case of large Q, the states at Fermi level get closer to the BZ boundary. Based on a second-order perturbation analysis, it is not difficult to find that the eigen energy near Fermi level for the case of large Q have a negative and nontrivial shift in the case of tilted Weyl cone. Such an argument can be further verified by observing the real-part of self-energy which gives just the modification to the eigen energy spectrum by the impurity scattering. The numerical results are shown in figures 6(c) and (d), where only the case of inra-valley scattering is shown since the inter-valley scattering has the analogous

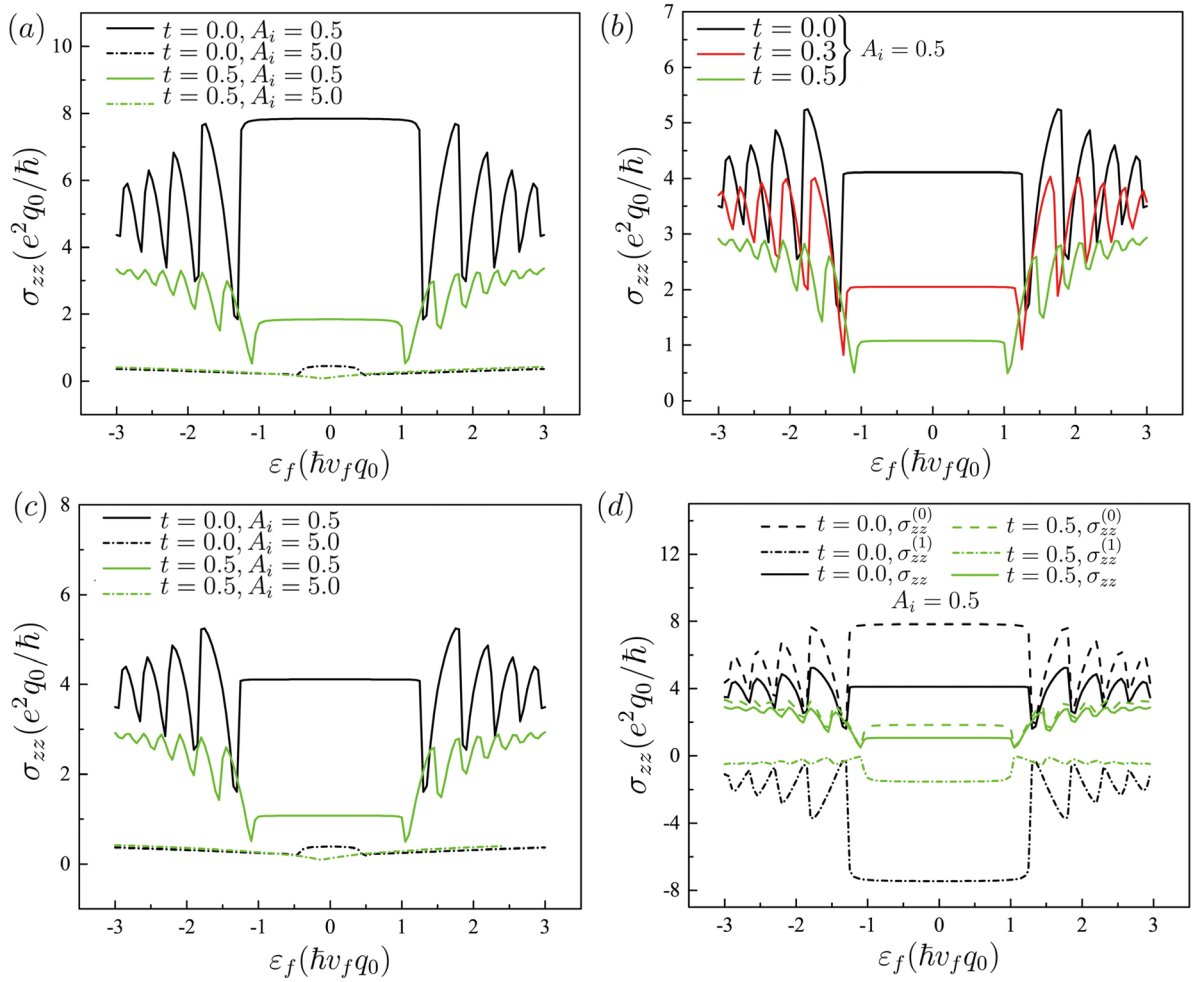

Figure 7. Longitudinal conductivity of a WSM for typical cases. (a) The contribution of the zero-order bubble diagram σ_{zz} are plotted for the cases with and without cone tilt, subject to weak and strong intra-valley scattering ($A_i = 0.5$ and 5.0). (b) Weak inter-valley scattering ($A_i = 0.5$) with different cone tilts of $t = 0.0$, 0.3 and 0.5. (c) A comparison of σ_{zz} spectra between strong and weak inter-valley scattering ($A_i = 0.5$ and 5.0), without and with cone tilt ($t = 0$ and 0.5). (d) The contributions to longitudinal conductivity of zero-order bubble diagram, denoted as $\sigma_{zz}^{(0)}$, and first-order bubble diagrams, denoted as $\sigma_{zz}^{(1)}$, are compared with σ_{zz} obtained within SCBA subject to weak inter-valley scattering.

effect. Indeed, as shown in figures 6(c) and (d), only when the Weyl cone get tilted, impurity scattering results in an appreciable negative modification on the Landau subbands.

In figure 7(a) the longitudinal conductivity spectra in the presence of intra-valley scattering, i.e. σ_{zz} as a function of ε_f, is plotted. But these numerical results are obtained by only taking into account the zero-order bubble diagram. If we include all bubble diagrams due to the intra-valley scattering to calculate σ_{zz} the numerical result tends to infinite. This just reflects the chiral anomaly characterized by the unidirectional propagation of the $n = 0$ subband. When a magnetic field is applied, the elastic intra-valley scattering is invalid, hence the resistivity vanishes. This implies an negative and very large magnetoresistance which is viewed as the signature of chiral anomaly in WSMs. Recently, there are more and more experimental observation of NLMR in realistic WSM materials [19, 22, 26, 29, 45]. Our numerical calculation indicates that the high-order scattering processes always play the essential role for the longitudinal conductivity even in the weak intra-valley scattering limit. We now turn to study the influence of the inter-valley scattering on the longitudinal conductivity. The numerical results are shown in figures 7(b)–(d). Unlike σ_{xx}, as shown in figures 7(b) and (c), σ_{zz} decreases with the increase of the cone tilt and inter-valley scattering strength. This is because that the longitudinal electronic transport behaves just like a 1D system with the subband structure as shown in figure 1(e). In this context, the impurity of inter-valley scattering plays a role of impeding electronic transport. Besides, the cone tilt makes electronic velocity in the chiral subband ($n = 0$) to descend. Therefore, σ_{zz} decreases with the increase of cone tilt and scattering strength. In order to clarify the role of high-order bubble diagrams on longitudinal conductivity, we calculate the contributions of zero- and first-order bubble diagram, denoted as $\sigma_{zz}^{(0)}$ and $\sigma_{zz}^{(1)}$ respectively, And then, we make a comparison between the two results with the calculated σ_{zz} within SCBA, namely, taking into account all the bubble diagrams as shown in figure 1(c). Such a comparison is shown in figure 7(d). We find that the zero-order contribution $\sigma_{zz}^{(0)}$ deviates obviously from the whole longitudinal conductivity, in particular, in the flat

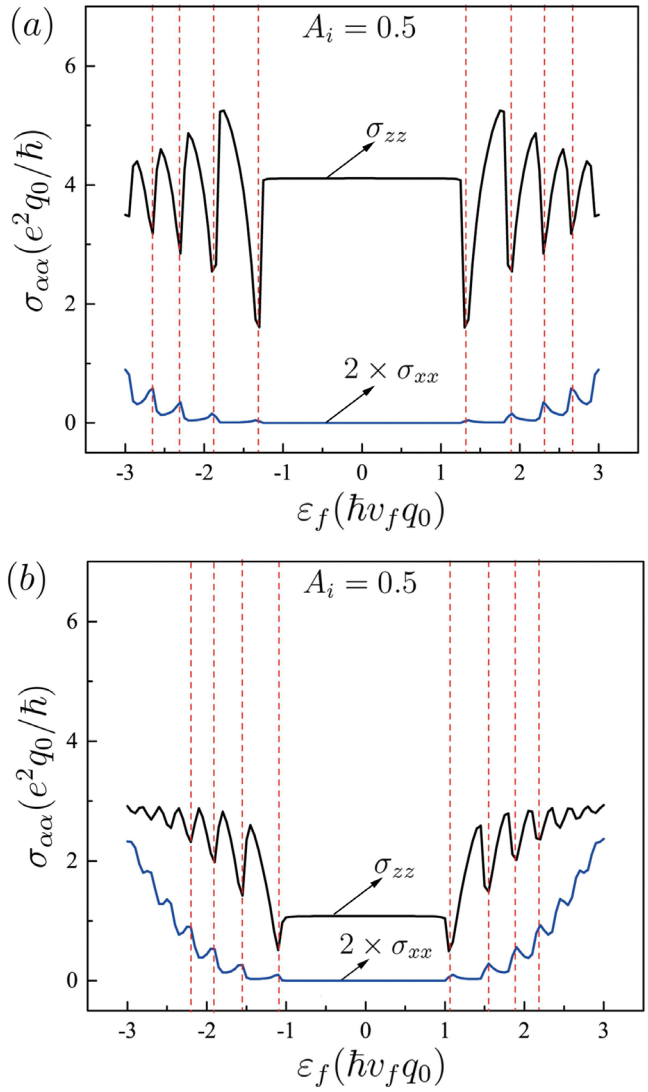

Figure 8. A comparison of σ_{xx} and σ_{zz} of (a) untilted ($t = 0.0$) and (b) tilted ($t = 0.5$) WSM under the weak inter-valley scattering.

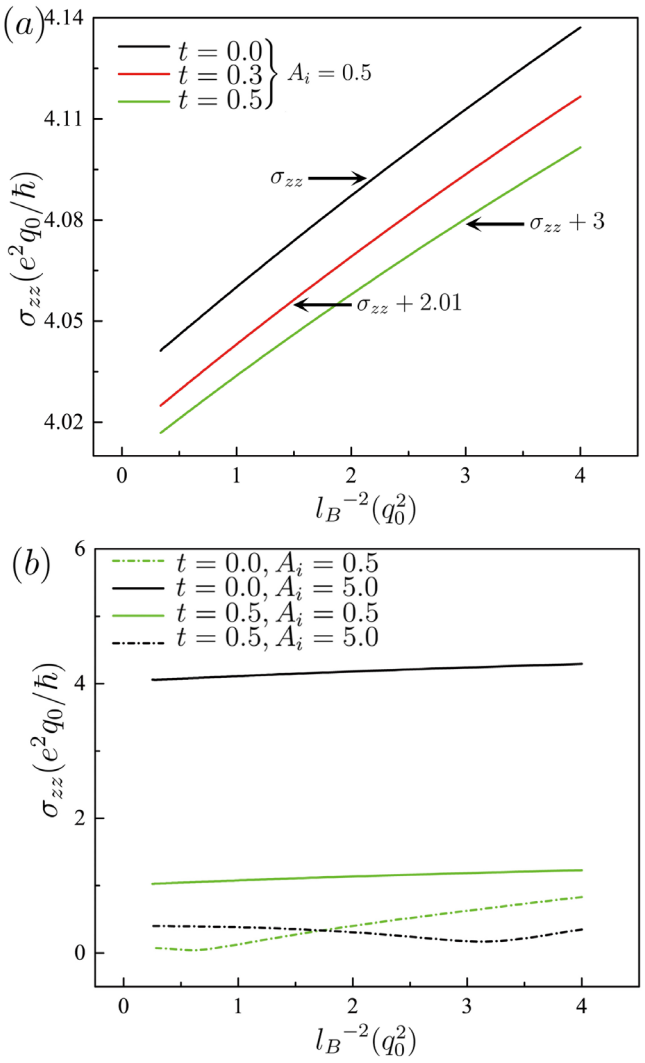

Figure 9. σ_{zz} versus l_B^{-2} (proportional to magnetic field strength) at zero energy ($\varepsilon_f = 0.0$). (a) Weak inter-valley scattering of $A_i = 0.5$ for the cases of cone tilt $t = 0.0$ and 0.3 and 0.5. In order to see the linear relationship clearly, we shifted the conductivity corresponding to $t = 0.3$ and $t = 0.5$ by $+2.01$ and $+3$, respectively. (b) A comparison of σ_{zz} versus l_B^{-2} as a function l_B^{-2} between the cases of weak and strong inter-valley scattering, without and with cone tilt ($t = 0$ and 0.5).

region around zero energy, even though the inter-valley scattering ($A_i = 0.5$) is so weak that the Landau level peaks are still distinguishable. More interestingly, the first-order contribution $\sigma_{zz}^{(1)}$ is negative, just opposite to the effect of inter-valley scattering on the transversal conductivity as mentioned above. When the cone tilt occurs, such a feature remains, it weakens though. From the result shown in figure 7(d) we can conclude that the high-order contributions of inter-valley scattering still play the essential role even in the weak scattering limit. In short, from the numerical results as shown in figure 7 we can conclude that the inter-valley scattering brings about a finite resistivity for the longitudinal electronic transport which is immune to the intra-valley scattering. And the high order bubble diagrams have the nontrivial effect on the longitudinal conductivity. To our knowledge, the influence of inter-valley scattering on the magnetoresistance of WSM begins to draw attention [46]. But the contribution of hight order terms must be treated carefully.

We make a comparison of the spectra between σ_{xx} and σ_{zz} in figures 8(a) and (b) for untiled and tilted WSMs respectively. What is interesting observed from figure 8 is that the peaks of transversal conductivity always correspond to the valleys of the longitudinal conductivity. As discussed above, the peaks of transversal conductivity and DOS spectra just coincide with each other. They occurs at the minima of subbands. However, the longitudinal conductivity can be viewed as a result of quantum transport of a 1D system with the Landau subbands. At the minima of subbands, the electronic velocity along z direction vanishes. Therefore, it is not surprising that σ_{zz} presents valleys at subband minima.

Finally, we turn to study the dependence of σ_{zz} on magnetic field strength subject to inter-valley scattering. The numerical result of σ_{zz} versus l_B^{-2} is shown in figure 9. One can see that at relatively weak scattering, as shown in figure 9(a), σ_{zz}

depends on l_B^{-2} linearly but very weakly. This implies that the inter-valley scattering only contributes the trivial part of longitudinal magnetoresistance, in contrast to the intra-valley scattering. Meanwhile, when the impurity scattering becomes strong, such a linear dependence is obviously destroyed. It is similar to the case of transversal conductivity as shown in figure 5. However, unlike the case of transversal conductivity, with the increase of scattering strength, σ_{zz} decreases.

4. Summary and discussion

Within the theoretical framework of Kubo formula and SCBA, we have studied the transversal and longitudinal magneto-conductivity of WSM described by a two-node Hamiltonian model. We focus mainly on the peculiar role of inter-valley scattering on LTMR and NLMR of type-I WSMs without and with cone tilt, in comparison with that of intra-valley scattering. We now summarize our main findings. At first, we find that the contributions of high-order Feynman diagrams to σ_{xx} play the distinct roles between the cases of intra- and inter-valley scatterings. The former suppresses the transversal conductivity whereas the latter enhances it. Then, with the increase of scattering strength, the LTMR is destroyed, accompanying a sizable increase of conductivity. Thirdly, for longitudinal electronic transport, the intra-valley scattering becomes invalid if all the Feynman diagrams within SCBA are taken into account. As a result, the longitudinal resistivity vanishes, which implies a very large NLMR. In addition, inter-valley scattering contributes only trivial magnetoresistance. More importantly, we find that the high-order Feynman diagrams always play the nontrivial role on the longitudinal conductivity even in the weak scattering limit where the self-energy arising from impurity scattering is far smaller than the Landau level spacing. Finally, we make a comparison between σ_{xx} and σ_{zz} spectra. It is found that the peaks of transversal conductivity always correspond to the valleys of the longitudinal conductivity.

Before ending this work, we would like to point out that all the calculations performed by us are restricted in the case of zero temperature. An extension of this work to finite temperature is straightforward within the theoretical framework of original Kubo formula. We have noticed that the magneto-transport properties of type-I Weyl semimetals at finite temperature subject to intra-valley scattering have been studied previously [39]. However, the effect of inter-valley scattering remains thus far intact, which is a topic left for future study.

Acknowledgments

This work was financially supported by the National Natural Science Foundation of China (Grant No. 11474122 and 11774123) and the National Science Foundation for Young Scientists of China (Grant No. 11404132, No. 11504125 and No. 11504319). We thank the High Performance Computing Center of Jilin University for their calculation resource.

ORCID iDs

Yisong Zheng https://orcid.org/0000-0003-2532-9171

References

[1] Yang K Y, Lu Y M and Ran Y 2011 *Phys. Rev.* B **84** 075129
[2] Wang Z, Gresch D, Soluyanov A A, Xie W, Kushwaha S, Dai X, Troyer M, Cava R J and Bernevig B A 2016 *Phys. Rev. Lett.* **117** 056805
[3] Autès G, Gresch D, Troyer M, Soluyanov A A and Yazyev O V 2016 *Phys. Rev. Lett.* **117** 066402
[4] Soluyanov A A 2015 *Nature* **527** 495
[5] Hu J, Xu S Y, Ni N and Mao Z 2019 *Annu. Rev. Mater. Res.* **49** 207
[6] Lv B Q *et al* 2015 *Phys. Rev.* X **5** 031013
[7] Xu S Y *et al* 2015 *Science* **349** 613
[8] Xu S Y, Alidoust N, Belopolski I, Yuan Z, Bian G, Chang T R, Hao Z, Strocov V N, Sanchez D S and Chang G 2015 *Nat. Phys.* **11** 748
[9] Xu S Y *et al* 2015 *Sci. Adv.* **1** 40
[10] Shekhar C, Nayak A K, Sun Y, Schmidt M, Nicklas M, Leermakers I, Zeitler U, Skourski Y, Wosnitza J and Liu Z 2015 *Nat. Phys.* **11** 645
[11] Wan X, Turner A M, Vishwanath A and Savrasov S Y 2011 *Phys. Rev.* B **83** 205101
[12] Ikhlas M, Tomita T, Koretsune T, Suzuki M T, Nishiohamane D, Arita R, Otani Y and Nakatsuji S 2017 *Nat. Phys.* **13** 1085–90
[13] Satoru N, Naoki K and Tomoya H 2015 *Nature* **527** 212
[14] Yang H, Sun Y, Zhang Y, Shi W J, Parkin S S P and Yan B 2017 *New J. Phys.* **19** 015008
[15] Kuroda K, Tomita T, Suzuki M T, Bareille C, Nugroho A A, Goswami P, Ochi M, Ikhlas M, Nakayama M and Akebi S 2017 *Nat. Mater.* **16** 1090
[16] Nakajima Y *et al* 2015 *Sci. Adv.* **1** e1500242
[17] Hirschberger M, Kushwaha S, Wang Z, Gibson Q, Liang S, Belvin C A, Bernevig B A, Cava R J and Ong N P 2016 *Nat. Mater.* **15** 1161–65
[18] Tian L, Quinn G and Ali M N 2015 *Nat. Mater.* **14** 280
[19] Li C Z, Wang L X, Liu H, Wang J, Liao Z M and Yu D P 2015 *Nat. Commun.* **6** 10137
[20] Burkov A A 2015 *J. Phys.: Condens. Matter* **27** 113201
[21] Ominato Y and Koshino M 2014 *Phys. Rev.* B **89** 054202
[22] Son D T and Spivak B Z 2013 *Phys. Rev.* B **88** 104412
[23] Altland A and Bagrets D 2015 *Phys. Rev. Lett.* **114** 257201
[24] Burkov A A 2015 *Phys. Rev.* B **91** 245157
[25] Syzranov S V, Radzihovsky L and Gurarie V 2015 *Phys. Rev. Lett.* **114** 166601
[26] Zyuzin V A 2017 *Phys. Rev.* B **95** 245128
[27] Abrikosov A A 1998 *Phys. Rev.* B **58** 2788
[28] Juyal A, Agarwal A and Mukhopadhyay S 2018 *Phys. Rev. Lett.* **120** 096801
[29] Niemann A C *et al* 2017 *Sci. Rep.* **7** 43394
[30] Feng J, Pang Y, Wu D, Wang Z, Weng H, Li J, Dai X, Fang Z, Shi Y and Lu L 2015 *Phys. Rev.* B **92** 081306
[31] Li Y, Wang Z, Li P, Yang X, Shen Z, Sheng F, Li X, Lu Y, Zheng Y and Xu Z A 2017 *Frontiers Phys.* **12** 127205
[32] Du J *et al* 2016 *Sci. China Phys. Mech. Astron.* **59** 657406
[33] Pan X C *et al* 2017 *Frontiers Phys.* **12** 127203
[34] Wang Y, Chen C H, Hu D, Ulmschneider M B and Ulmschneider J P 2016 *Nat. Commun.* **7** 13535
[35] Das K and Agarwal A 2019 *Phys. Rev.* B **99** 085405
[36] Xiao X, Law K T and Lee P A 2017 *Phys. Rev.* B **96** 165101
[37] Shao J and Yan L 2019 *AIP Adv.* **9** 045319
[38] Ramakrishnan N, Milletari M and Adam S 2015 *Phys. Rev.* B **92** 245120

[39] Klier J, Gornyi I V and Mirlin A D 2017 *Phys. Rev.* B **96** 214209
[40] Bastin A, Lewiner C, Betbeder-matibet O and Nozieres P 1971 *J. Phys. Chem. Solids* **32** 1811
[41] Crépieux A and Bruno P 2001 *Phys. Rev.* B **64** 014416
[42] Klier J, Gornyi I V and Mirlin A D 2015 *Phys. Rev.* B **92** 205113
[43] Pesin D A, Mishchenko E G and Levchenko A 2015 *Phys. Rev.* B **92** 174202
[44] Behrends J, Kunst F K and Sbierski B 2018 *Phys. Rev.* B **97** 064203
[45] Huang X *et al* 2015 *Phys. Rev.* X **5** 031023
[46] Ji X T, Lu H Z, Zhu Z G and Su G 2017 *AIP Adv.* **7** 105003